INVITED PAPER

Azimuthal instability of a vortex ring computed by a vortex sheet panel method

Hualong Feng[1], Leon Kaganovskiy[2] and Robert Krasny[3]

[1] School of Science, Nanjing University of Science and Technology, Nanjing, Jiangsu 210094, People's Republic of China
[2] Department of Natural Sciences, New College of Florida, Sarasota, FL 34243, USA
[3] Department of Mathematics, University of Michigan, Ann Arbor, MI 48109, USA

E-mail: krasny@umich.edu

Abstract

A Lagrangian panel method is presented for vortex sheet motion in three-dimensional (3D) flow. The sheet is represented by a set of quadrilateral panels having a tree structure. The panels have active particles that carry circulation and passive particles used for adaptive refinement. The Biot–Savart kernel is regularized and the velocity is evaluated by a treecode. The method is applied to compute the azimuthal instability of a vortex ring, starting from a perturbed circular disc vortex sheet initial condition. Details of the core dynamics are clarified by tracking material lines on the sheet surface. Results are presented showing the following sequence of events: spiral roll-up of the sheet into a ring, wavy deformation of the ring axis, first collapse of the vortex core in each wavelength, second collapse of the vortex core out of phase with the first collapse, formation of loops wrapped around the core and radial ejection of ringlets. The collapse of the vortex core is correlated with converging axial flow.

1. Introduction

Vortex rings are readily formed by ejecting fluid from a circular nozzle. At early times the ring maintains axisymmetry, but at later times it often undergoes a wavy azimuthal instability and abrupt transition to turbulence. A detailed understanding of this process is still being pursued by many investigators. The present work is concerned with numerical simulation of the azimuthal instability using a vortex sheet model for the ring. Comprehensive reviews on vortex rings were given by Shariff and Leonard (1992) and Lim and Nickels (1995). First, we briefly recall some of the relevant prior results, starting with experiments and proceeding to theory and numerical simulations.

Experimental visualization of the azimuthal instability must contend with the fact that the ring translates in space as the instability develops, but nonetheless many detailed features have been revealed. Maxworthy (1977) found that axial flow develops along the core of the ring due to azimuthal pressure gradients arising from non-uniform breakdown of the azimuthal waves. Glezer and Coles (1990) inferred that secondary vortex tubes with alternating circulation are wrapped around the core of the ring. Weigand and Gharib (1994) observed vortex shedding from the periphery of the ring accompanied by a stepwise decrease in ring circulation. Naitoh *et al* (2002) found that the deformation of the ring axis is correlated with axial flow in the core. Dazin *et al* (2006a, 2006b) documented many aspects of the linear and nonlinear stages of the instability, including the presence of secondary dipole structures in slices through the ring.

Theoretical analysis of the azimuthal instability is complicated by the curvature of the ring axis, but the case of a straight vortex tube offers a starting point. For example, Moore and Saffman (1975) performed a stability analysis of a vortex tube in an external strain field. From such studies emerged the idea that the azimuthal ring instability involves a competition between the irrotational strain induced by distant portions of the ring and the self-induced rotation of the core. Widnall and co-workers presented a series of papers culminating in the work of Widnall and Tsai (1977), which gave predictions for the instability wavenumber, growth rate and mode structure in good agreement with experiment. Saffman (1978) studied the effect of the core vorticity profile and derived a formula for the instability wavenumber as a function of Reynolds number. Recent work by Fukumoto and Hattori (2005) showed that the ring's self-induced dipole field may have an even greater effect than the strain field in destabilizing the ring.

Numerical simulation of the azimuthal ring instability has been carried out using finite-differences (e.g. Archer *et al* 2008, Shariff *et al* 1994) and vortex methods (e.g. Bergdorf *et al* 2007, Cocle *et al* 2008, Knio and Ghoniem 1990). In most cases the initial condition is a toroidal core to which a perturbation is applied. The present work instead uses a vortex sheet model encompassing the spiral roll-up by which the core of the ring is formed. In addition, we use free-space boundary conditions (i.e. the velocity vanishes far from the ring) instead of the periodic boundary conditions common in previous simulations.

Vortex methods were reviewed by Cottet and Koumoutsakos (2000). A numerical method for tracking vortex sheet motion in three-dimensional (3D) flow requires a discrete representation of the sheet, a quadrature scheme for evaluating the Biot–Savart integral and an adaptive refinement scheme to maintain resolution as the sheet rolls up. Triangulations are often used to represent the sheet surface (e.g. Agishtein and Migdal 1989, Brady *et al* 1998, Pozrikidis 2000, Stock 2006, Stock *et al* 2008), but filament representations have also been employed (e.g. Ashurst and Meiburg 1988, Lindsay and Krasny 2001, Sakajo 2001). A variety of quadrature and adaptive refinement schemes have been developed, and this is still an active area of research.

The present approach uses a Lagrangian panel method that builds on previous work, but also incorporates some new techniques (Kaganovskiy 2006, 2007, Feng 2007). Panel methods are often used in aerodynamics to treat unsteady free vortex sheets as well as bound vortex sheets on solid surfaces (Katz and Plotkin 2001). Here, we regularize the Biot–Savart kernel and use a treecode to evaluate the velocity, following Lindsay and Krasny (2001), but instead of the filament representation used there, we employ a panel representation that is more effective in resolving the deformed sheet surface. Each panel is a quadrilateral patch with respect to Lagrangian coordinates. The set of all panels has a quadtree structure distinct from the octtree structure used in the treecode. The panels have active particles that carry circulation and passive particles used for adaptive refinement. The refinement scheme tests

2

each panel for deformation and if necessary subdivides the panel into four subpanels. New particles are inserted by interpolation with respect to Lagrangian coodinates (Krasny 1987). The quadrature scheme evaluates the circulation element using differences of the flow map. The numerical method is local in the sense that it requires little communication between neighboring panels.

The method is applied to compute the azimuthal instability of a vortex ring, starting from a perturbed circular disk vortex sheet initial condition. Details of the core dynamics are clarified by tracking material lines on the sheet surface. Results are presented showing the following sequence of events. Initially the edge of the sheet rolls up into a spiral core, effectively forming a perturbed vortex ring. While this is happening, the azimuthal waves steepen, leading to a collapse of the core in each wavelength. Afterward, a second collapse occurs out of phase with the first collapse, accompanied by the formation of loops wrapped around the core and radial ejection of ringlets. The collapse of the vortex core is correlated with converging axial flow, possibly as in the experiments of Naitoh *et al* (2002). Slices through the sheet surface reveal dipole structures, possibly resembling those observed by Dazin *et al* (2006a, 2006b).

The paper is organized as follows. Section 2 presents the vortex sheet evolution equation. Section 3 describes the numerical method. Section 4 presents numerical results. Conclusions are given in section 5.

2. Vortex sheet evolution equation

Following Caflisch (1988) and Kaneda (1990), we present the evolution equation for vortex sheet motion in 3D flow. The starting point is the Biot–Savart integral for the velocity induced by a vortex sheet,

$$u(x) = \int_S K(x, y) \times d\Gamma(y), \tag{1}$$

where S is the sheet surface, $d\Gamma$ is the vector-valued circulation element on the sheet and

$$K(x, y) = -\frac{x - y}{4\pi |x - y|^3} \tag{2}$$

is the Biot–Savart kernel. Note that

$$d\Gamma = (n \times U)dS, \tag{3}$$

where n is a unit normal vector on the sheet, U is the jump in velocity across the sheet and dS is a scalar area element on the surface. In computations it is advantageous to regularize the kernel and we employ the form suggested by Rosenhead (1930) and Moore (1972),

$$K_\delta(x, y) = -\frac{x - y}{4\pi (|x - y|^2 + \delta^2)^{3/2}}, \tag{4}$$

where δ is a smoothing parameter. Chorin and Bernard (1973) used a similar approach to compute vortex sheet motion in 2D flow.

We assume the sheet is a parametrized surface,

$$x = x(\alpha, \beta, t), \tag{5}$$

(a)   (b)   (c)
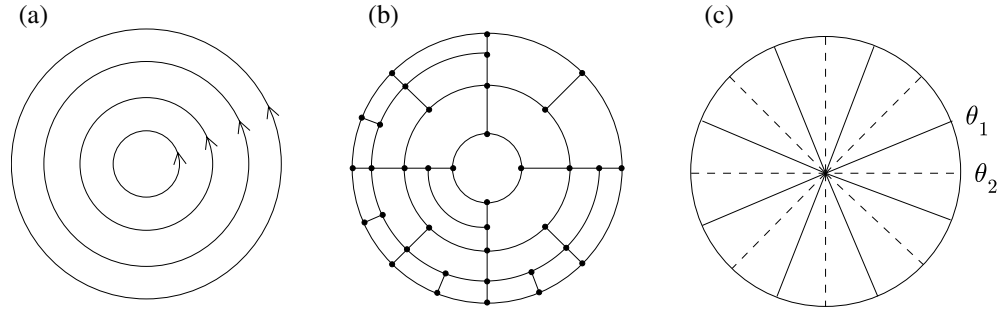
Figure 1. Schematic of circular disk vortex sheet: (a) vortex filaments, (b) panel representation, (c) azimuthal angles $\theta_1 = \frac{\pi}{8} \bmod \frac{\pi}{4}$ (solid lines), $\theta_2 = 0 \bmod \frac{\pi}{4}$ (dashed lines).

with Lagrangian coordinates α, β. We also refer to $\boldsymbol{x}(\alpha, \beta, t)$ as the flow map of the vortex sheet. Caflisch (1988) and Kaneda (1990) derived the following expression for the circulation element,

$$\mathrm{d}\boldsymbol{\Gamma} = \left(\frac{\partial \Gamma}{\partial \alpha} \frac{\partial \boldsymbol{x}}{\partial \beta} - \frac{\partial \Gamma}{\partial \beta} \frac{\partial \boldsymbol{x}}{\partial \alpha} \right) \mathrm{d}\alpha \, \mathrm{d}\beta, \tag{6}$$

where $\Gamma = \Gamma(\alpha, \beta)$ is the scalar circulation on the sheet and the Lagrangian derivatives of the flow map, $\partial \boldsymbol{x}/\partial \alpha$, $\partial \boldsymbol{x}/\partial \beta$, account for vortex stretching. In the present application to vortex rings, the vortex filaments are assumed to be closed curves and we take $\alpha = \Gamma$, $\beta = \theta$, where the circulation is normalized so that $0 \leqslant \Gamma \leqslant 1$ and θ is an angle variable along the filaments with $0 \leqslant \theta \leqslant 2\pi$. This yields

$$\mathrm{d}\boldsymbol{\Gamma} = \frac{\partial \boldsymbol{x}}{\partial \theta} \mathrm{d}\Gamma \mathrm{d}\theta \tag{7}$$

as a special case of equation (6). Finally, we have the vortex sheet evolution equation,

$$\frac{\partial \boldsymbol{x}}{\partial t} = \int_0^{2\pi} \int_0^1 \boldsymbol{K}_\delta(\boldsymbol{x}, \tilde{\boldsymbol{x}}) \times \mathrm{d}\tilde{\boldsymbol{\Gamma}}, \tag{8}$$

a form of equation (1) expressing the idea that the sheet advects in its self-induced velocity field.

3. Numerical method

In this section, we describe first the panel representation of the vortex sheet, then the quadrature and adaptive refinement schemes, and finally some coding details.

3.1. Panel representation

Consider Cartesian coordinates $\boldsymbol{x} = (x, y, z)$, where the z-direction is vertical. Figure 1a depicts a circular disc vortex sheet defined by

$$x = \sqrt{1 - \Gamma^2} \cos \theta, \quad y = \sqrt{1 - \Gamma^2} \sin \theta, \quad z = 0, \tag{9}$$

where $0 \leqslant \Gamma \leqslant 1$, $0 \leqslant \theta \leqslant 2\pi$. The sheet is comprised of circular vortex filaments, i.e. lines on which the circulation Γ is constant. Equation (9) corresponds to the bound vortex sheet

(a)

(b)
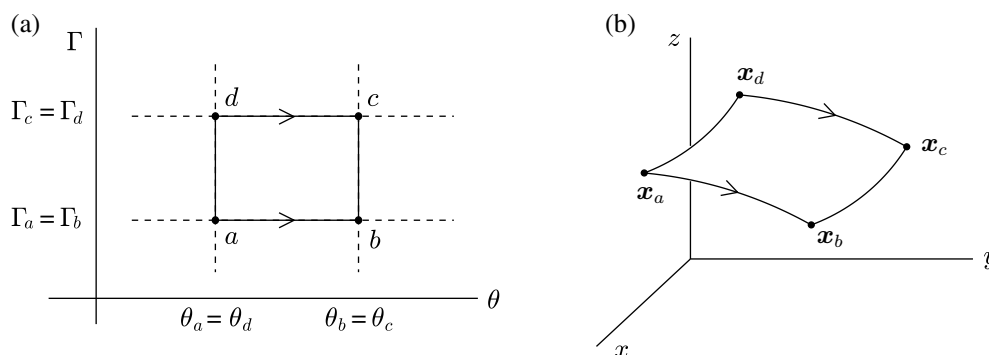
Figure 2. Definition of a panel. (a) Panel in Lagrangian coordinate space with vertices a, b, c, d and (b) the same panel in physical space with vertices $\boldsymbol{x}_a$, $\boldsymbol{x}_b$, $\boldsymbol{x}_c$, $\boldsymbol{x}_d$. Arrows indicate panel edges corresponding to vortex filaments.

in potential flow past a circular disk, and if the sheet is allowed to roll up, it forms an axisymmetric vortex ring (Taylor 1953). The initial condition for the simulation includes a perturbation in the z-coordinate, leading to a non-axisymmetric ring. Figure 1(b) is a schematic of the panel representation of the sheet. A panel is a quadrilateral patch on the sheet surface with particles at the vertices. The panels cover the sheet and the set of all panels has a quadtree structure created by adaptive refinement, as explained below. For future reference, in figure 1(c) we define two sets of azimuthal angles, $\theta_1 \equiv \frac{\pi}{8} \bmod \frac{\pi}{4}$ and $\theta_2 \equiv 0 \bmod \frac{\pi}{4}$; in the example computed later below, θ_1 corresponds to the crests and θ_2 corresponds to the troughs of the perturbation in the direction of ring propagation.

Figure 2 gives more detail about the definition of a panel. Figure 2(a) depicts a panel in Lagrangian coordinate space with vertices a, b, c, d. A panel is a rectangle with sides parallel to the coordinate axes, so that either $\Gamma = $ constant or $\theta = $ constant on each edge. The lines of constant Γ, indicated by arrows, correspond to vortex filaments. Figure 2(b) depicts the panel in physical space with particles $\boldsymbol{x}_a$, $\boldsymbol{x}_b$, $\boldsymbol{x}_c$, $\boldsymbol{x}_d$ at the vertices. The particles are advected in physical space and the panel retains its definition as a rectangular patch in Lagrangian coodinate space.

3.2. Quadrature scheme

Let $\boldsymbol{x}_i, i = 1 : N$ denote the set of all particles on the sheet. We need to explain how the particle velocities are computed. The method is conceptually simple; the integral over the sheet surface in equation (8) is replaced by a sum over panels and the integral over each panel is evaluated by a 2D trapezoid rule. This leads to a discretization of the form

$$\frac{\mathrm{d}\boldsymbol{x}_i}{\mathrm{d}t} = \sum_{j=1}^{N} \boldsymbol{K}_\delta(\boldsymbol{x}_i - \boldsymbol{x}_j) \times \boldsymbol{w}_j, \tag{10}$$

where $\boldsymbol{w}_j$ is the weight associated with particle $\boldsymbol{x}_j$. The weights are given in terms of the circulation elements $\mathrm{d}\boldsymbol{\Gamma}$ and we refer to figure 2 to explain how these are computed. One approach, based on equation (7), has the general form

$$\mathrm{d}\boldsymbol{\Gamma} \approx \left(\frac{\partial \boldsymbol{x}}{\partial \theta}\right)_v \cdot (\Gamma_d - \Gamma_a)(\theta_b - \theta_a), \tag{11}$$
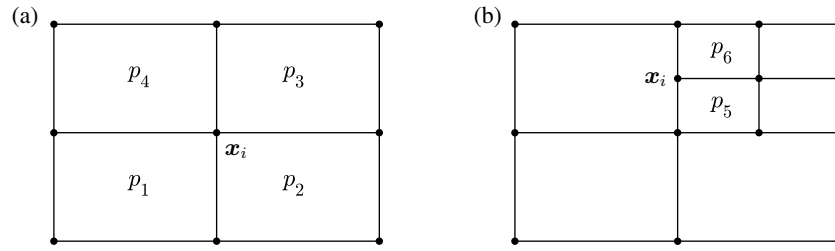
Figure 3. Assigning particle weights, two cases. (a) Particle x_i receives weight from panels p_1, p_2, p_3, p_4, and (b) particle x_i receives weight from panels p_5, p_6.
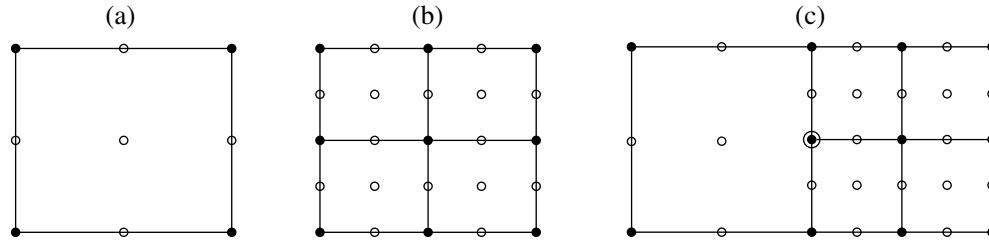
Figure 4. Adaptive refinement scheme: (a) a panel has active particles (●) and passive particles (○), (b) the original panel has been subdivided into four subpanels and (c) adjacent panels can reside at different levels of subdivision; the particle labeled ⊙ is passive for the left panel and active for the two right subpanels of which it is a vertex.

where $(\partial x/\partial\theta)_v$ is a finite-difference approximation to the partial derivative of the flow map at a given vertex v of the panel. This approach was employed by Kaganovskiy (2006), but he used a finite-difference formula requiring information from neighboring panels to compute $(\partial x/\partial\theta)_v$ and found that accuracy was lost as the sheet surface became increasingly deformed. Feng (2007) proposed a simple alternative,

$$d\mathbf{\Gamma} \approx \left(\frac{x_b+x_c}{2} - \frac{x_a+x_d}{2}\right)(\Gamma_d - \Gamma_a), \tag{12}$$

which does not require information from neighboring panels, and this is the form used here. Hence the vertices of the panel are assigned weights

$$w_a = w_b = w_c = w_d = \tfrac{1}{4}d\mathbf{\Gamma}, \tag{13}$$

where $d\mathbf{\Gamma}$ is given by equation (12). The factor $\frac{1}{4}$ amounts to applying a 2D trapezoid rule for the integral over a panel.

Note that each panel gives rise to particle weights in this manner. The code therefore loops over the panels and assigns weight to the panel vertices. Figure 3 depicts two cases. The typical case is that a particle receives weight from four panels (figure 3(a)), but some particles receive weight from only two panels (figure 3(b)). This concludes our discussion of the particle weights in equation (10).

3.3. Adaptive refinement scheme

At this point we note that the code actually advects two types of particles, denoted *active* and *passive*. The active particles are the ones dealt with up to now and the passive particles are a new type used for adaptive refinement. Figure 4(a) shows a panel with active particles (●) at
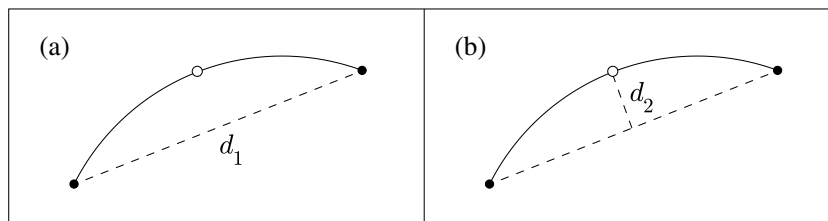
Figure 5. Distances in physical space used to flag panels for refinement. (a) d_1: chord length of edge and (b) d_2: distance from passive particle to chord midpoint.

the vertices and passive particles ($\circ$) at the midpoints of the edges and the panel interior. We emphasize that these are midpoints with respect to Lagrangian coordinates. For example with reference to the panel in figure 2, a passive particle at the midpoint of edge ab has Lagrangian coordinates $(\Gamma, \theta) = (\Gamma_a, \frac{1}{2}(\theta_a + \theta_b))$, and in physical space it lies somewhere on the arc $\boldsymbol{x}_a\boldsymbol{x}_b$. The active particles contribute circulation to the quadrature scheme through equation (12), as previously described. The passive particles do not contribute circulation, but instead enable us to account for panel curvature in the refinement scheme. We explain their role below.

When a panel is flagged for refinement, it is subdivided into four subpanels as in figure 4(b). In this case, the passive particles in the original panel become active particles in the subpanels, and new passive particles are inserted in the subpanels by quadratic interpolation with respect to Lagrangian coordinates. For example, along the panel edge where $\Gamma = \Gamma_a = \Gamma_b$ in figure 2, there are two active particles (with $\theta = \theta_a, \theta_b$) and one passive particle (with $\theta = \frac{1}{2}(\theta_a + \theta_b)$); this information is used to insert passive particles at the midpoints of the subpanel edges by quadratic interpolation with respect to θ. Also note that the code allows adjacent panels to reside at different levels of subdivision, as in figure 4(c). In this case the particle labeled $\odot$ is passive for the left panel and active for the two right subpanels of which it is a vertex.

Finally we need to explain how a panel is flagged for refinement. This is done by testing the panel edges using the distances in physical space defined in figure 5. For each edge we compute d_1 (chord length) and d_2 (distance from passive particle to chord midpoint). If d_1 or d_2 exceeds a user-specified tolerance, the panels on either side of the edge are subdivided. Distance d_1 acts in regions where the sheet is being stretched and distance d_2 acts in regions of high curvature. This concludes our discussion of the adaptive refinement scheme.

3.4. Coding details

As explained above, the sheet is represented by a set of panels and particles. A particle has Cartesian coordinates $\boldsymbol{x}_i = (x_i, y_i, z_i)$, Lagrangian coordinates (Γ_i, θ_i) and quadrature weight $\boldsymbol{w}_i$, and the code uses global linear arrays to store this information. There is also a quadtree data structure for the panels, with each node containing information about a given panel, e.g. level of the panel in the quadtree, pointers to subpanels, flags for panel refinement and indices in the global particle arrays of the particles belonging to the panel. The panel quadtree is created at time $t = 0$ and is updated at each time step by the refinement scheme.

Each edge belongs to two adjacent panels (except for edges on the boundary of the sheet) and when a new passive particle is inserted on an edge, that information needs to be communicated to the two panels on either side of the edge. To find these panels, a recursive search of Lagrangian coordinate space is performed using a bisection method. The cost of the search is logarithmic in the number of panels.
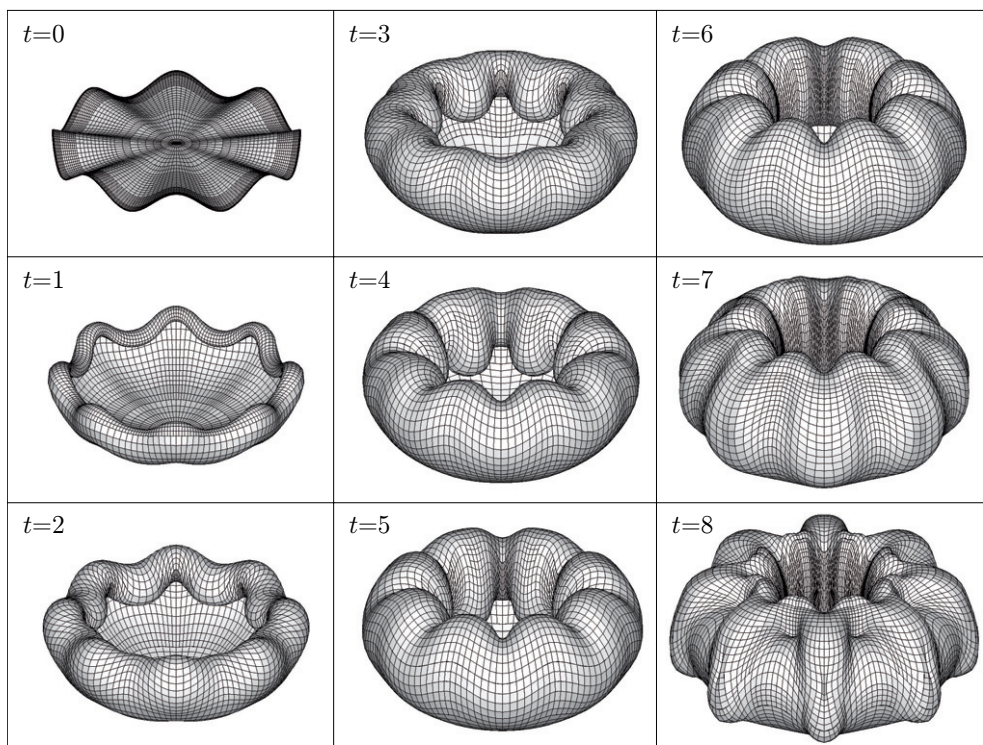
Figure 6. Vortex sheet roll-up into a vortex ring. The panels representing the sheet surface are plotted as a wire mesh.

The code was written in Fortran90. There are two components, a main program and the treecode subroutine. The main program controls input, output, timestepping and refinement. The treecode subroutine computes the velocity of the particles using the method described by Lindsay and Krasny (2001). The Fortran90 treecode subroutine is based on code for electrostatics (Johnston). The quadtree structure of the panels is distinct from the octtree structure of the particle clusters in the treecode. The results are visualized using Tecplot.

4. Numerical results

The panel method was applied to compute an example of vortex sheet roll-up into a vortex ring. A perturbation of the form $z = ar^2\cos k\theta$ was imposed on the circular disk vortex sheet in equation (9), where (r, θ) are polar coordinates on the unperturbed sheet (the factor r^2 ensures that the perturbation is concentrated near the edge of the disk). The perturbation amplitude was $a = 0.1$ the azimuthal wavenumber was $k = 8$, the smoothing parameter was $\delta = 0.1$ and the fourth-order Runge–Kutta method with $\Delta t = 0.05$ was used for timestepping. The tolerances for panel refinement were $d_1 \leqslant 0.2$ (chord length) and $d_2 \leqslant 0.02$ (midpoint-chord distance). The treecode used $p_{\max} = 8$ (maximum order), $\epsilon = 10^{-5}$ (error tolerance) and $N_0 = 1000$ (maximum number of particles in a leaf of the tree). Refinement tests were performed to ensure that the results are well-resolved. The initial condition has eight-fold symmetry and although this was not imposed in the simulation, it was preserved to a high degree of accuracy.
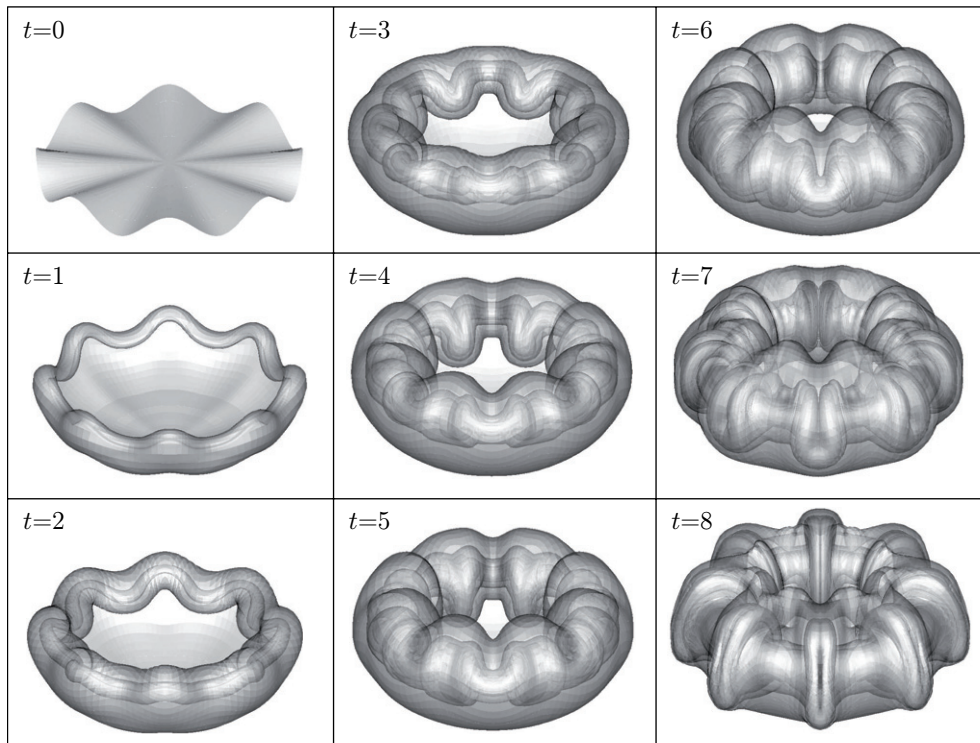
Figure 7. Vortex sheet plotted as a translucent surface, permitting a view of the core.

The computation was stopped at $t = 8$ when the sheet had become highly distorted. At $t = 0$ there were 2004 active particles and 7785 passive particles, and at $t = 8$ there were 274 628 active particles and 1 117 875 passive particles. The code was compiled using gfortran. The computation was performed on a Mac PowerPC G5 computer and required 52 h of CPU time.

Figure 6 plots the panels representing the sheet surface as a wire mesh. Initially the sheet is a circular disk with a wavy perturbation in the z-coordinate. At early times the edge of the sheet rolls up into a spiral, effectively forming a perturbed vortex ring. The ring propagates in the negative z-direction, and recalling figure 1(c), this means that angles θ_1 correspond to the crests and angles θ_2 correspond to the troughs of the perturbation in the direction of ring propagation. The outer surface of the ring is smooth up to $t = 6$, but some wrinkling is evident at $t = 7$, and this becomes more pronounced at $t = 8$. As we shall see, there are complex dynamical events occurring inside the ring.

Figure 7 plots the sheet as a translucent surface, permitting a view of the core. At $t = 2$ the core is still a smooth wavy tube, but the waves are steepening and by $t = 5$, a folding of the core or *collapse* occurs at angles θ_1 around the ring. Details of the collapse will be shown in subsequent figures. This is followed at $t = 6$ by a second collapse at angles θ_2 around the ring, out of phase with the first collapse. The second collapse is accompanied by the formation of loops wrapped around the core. The loops become more narrow and stretched at $t = 7$ and 8.

Figure 8 plots three isosurfaces of vorticity, high (red), medium (blue) and low (green). In principle, the vorticity associated with a vortex sheet is a delta-function, but the regularization of the Biot–Savart kernel, equation (4), yields a smooth vorticity distribution from which

9
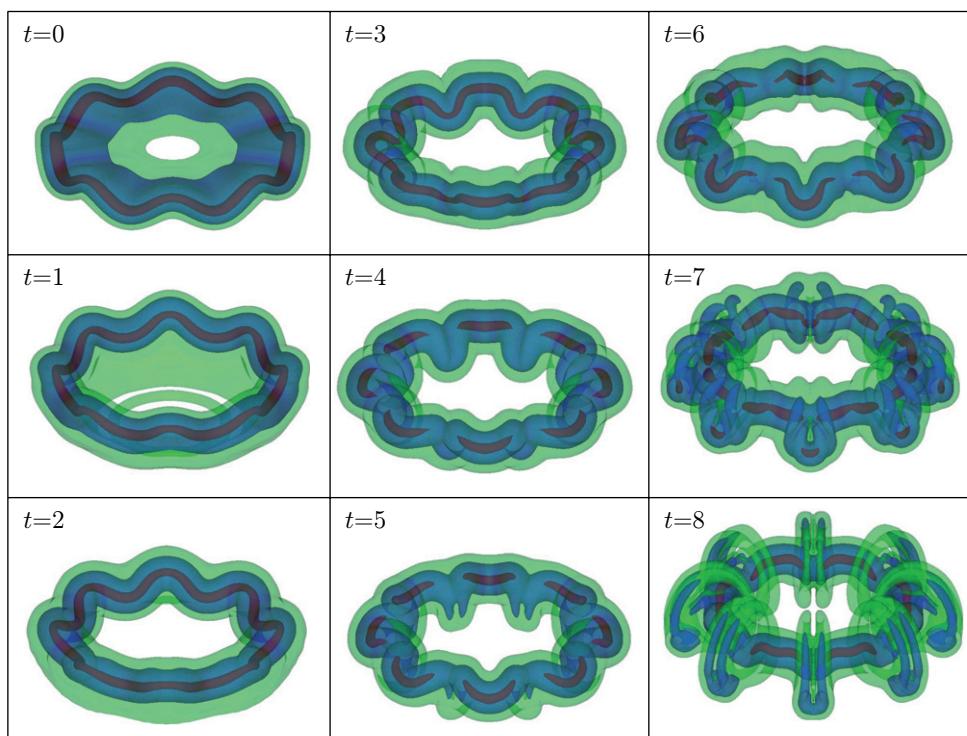
Figure 8. Vorticity isosurfaces: high (red), medium (blue), low (green). A smooth vorticity distribution is obtained due to the regularization of the Biot–Savart kernel, equation (4).

isosurfaces can be obtained. At early times the red isosurface representing the core is a smooth wavy tube, but at $t = 4$ it is disconnected at angles θ_1, the site of the first collapse. At $t = 8$ the red isosurface has reconnected at angles θ_1, but it is disconnected at angles θ_2, the site of the second collapse. At $t = 8$ the blue isosurface defines a connected central core, with a disconnected portion present in the loops wrapped around the core. The green isosurface forms a sheath around the entire structure.

Figure 9 plots a set of material lines. The black line at the edge of the sheet rolls up into the core and is referred to as the core filament. At $t = 0$ it has a wavy perturbation. Also plotted are red and blue lines that were initially rays (radial line segments). The blue lines are at angles θ_1 and the red lines are at angles θ_2. The red and blue lines roll up into spirals around the core filament, but they remain in a plane due to the symmetry of the perturbation. At $t = 5$ a hairpin forms in the core filament at angles θ_1, corresponding to the first collapse of the core. At this time the core filament is still smooth at angles θ_2, but it becomes semi-circular there at $t = 6$ and undergoes severe distortion at $t = 7$ and $t = 8$, corresponding to the second collapse of the core. At $t = 8$ the core of the red spiral is ejected radially.

Figure 10 plots vertical planar cross sections of the sheet containing the red and blue material lines. In an axisymmetric problem, the red and blue lines would be identical and indeed they are similar up to $t = 2$. Thereafter for $2 \leqslant t \leqslant 6$ the outer turn of the blue spiral grows more rapidly and its core is more distorted, in comparison with the red spiral. This is the effect of the first collapse, which is centered in the plane of the blue spiral. For $6 \leqslant t \leqslant 8$ the situation is reversed, as the outer turn of the red spiral grows rapidly and its core is distorted.
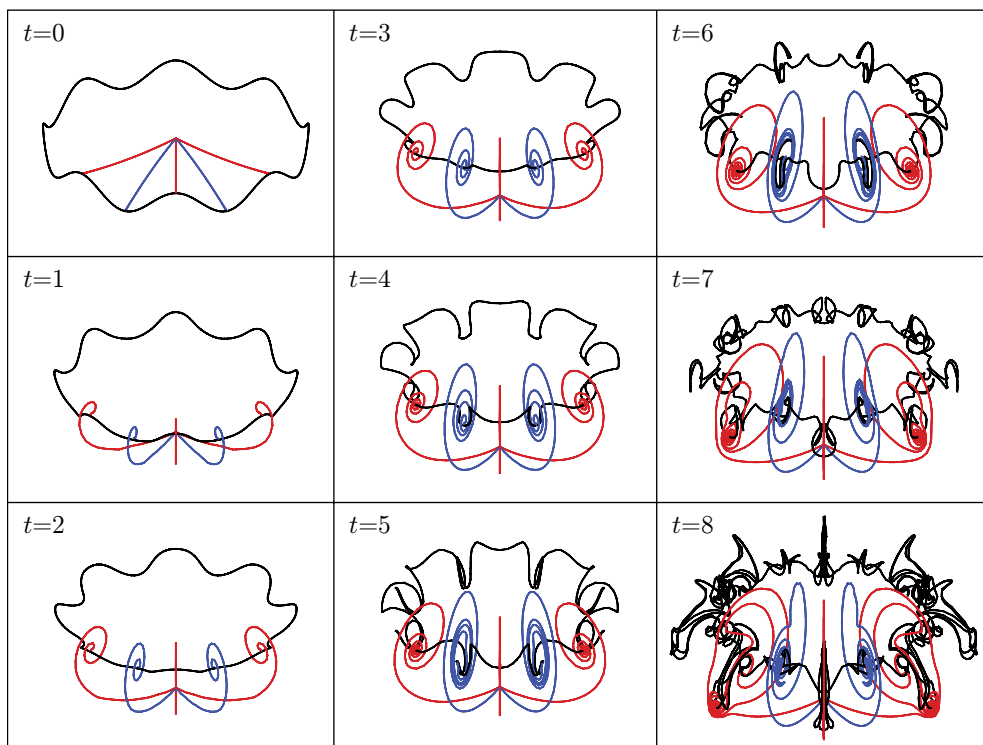
Figure 9. Core filament and rays. The black line is the vortex filament at the edge of the sheet and the red and blue lines are material lines that were initially rays (radial line segments).

This is the effect of the second collapse, which is centered in the plane of the red spiral. At $t = 8$ the core of the red spiral is ejected radially.

Figure 11 plots a top view of the core filament (black line), the red and blue lines, and now also a green line initially midway between the red and blue lines. The red and blue lines remain in a plane, as noted before, but the green lines can move within each azimuthal wavelength. Up to $t = 3$ the green lines stay away from the red and blue lines, but at $t = 4$ the green lines approach the adjacent blue lines along the core filament. This is an indication of axial flow in the vortex core, consistent with the findings of Naitoh *et al* (2002), and in fact we were motivated to plot these material lines by their experiments in which they used smoke to detect axial flow in the core. At $t = 7$ the situation changes as the green lines now approach the adjacent red lines and stay away from the blue lines. This means that the axial flow reverses direction in each wavelength between $t = 4$ and $t = 7$. Hence we see that the two successive collapses are correlated with local axial flow converging to the planes at angles θ_1 and θ_2, respectively. Figure 11 also supports the finding that ringlets are ejected radially at $t = 8$.

Figure 12 plots a top view of horizontal slices through the vortex core. A slice is the intersection of the sheet surface with a plane and it appears as a set of line segments. This diagnostic was motivated by the flow visualizations of Dazin *et al* (2006a, 2006b). They observed dipole structures on the periphery of the ring and we find similar features in figure 12. In the present case we infer that the dipole structures are cross-sections of the loops wrapped around the core.
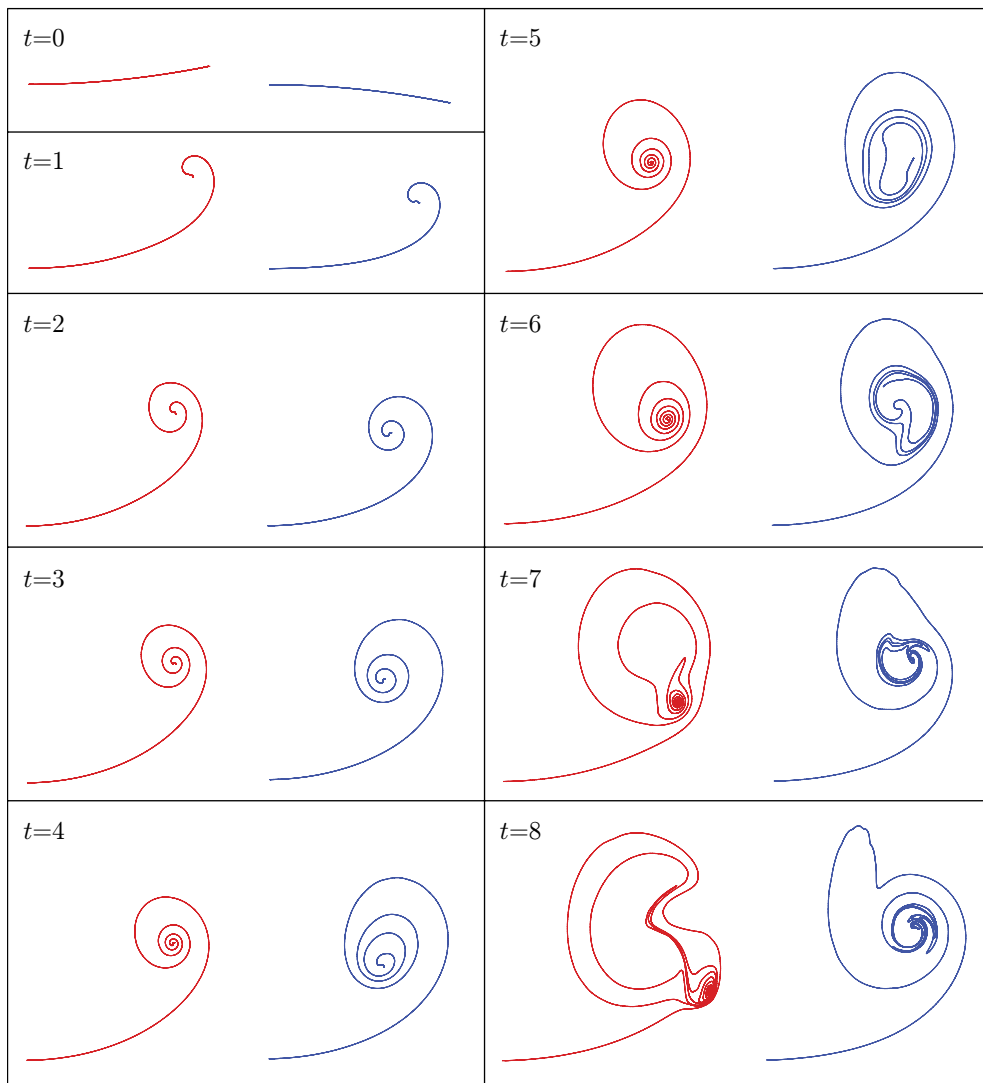
Figure 10. Planar cross sections through the sheet. The blue line is in the plane of the first collapse and the red line is in the plane of the second collapse.

5. Conclusions

A Lagrangian panel method was presented for vortex sheet roll-up in 3D flow. The method employs some common previous techniques such as regularizing the Biot–Savart integral and using a treecode to evaluate the velocity, but it also incorporates some new techniques: (i) representing the sheet by a set of quadrilateral panels having a tree structure, (ii) using passive particles to account for panel curvature in the refinement scheme and (iii) evaluating the circulation element by equation (12).

Results were presented for the azimuthal instability of a vortex ring starting from a perturbed circular disk vortex sheet initial condition. Details of the core dynamics were
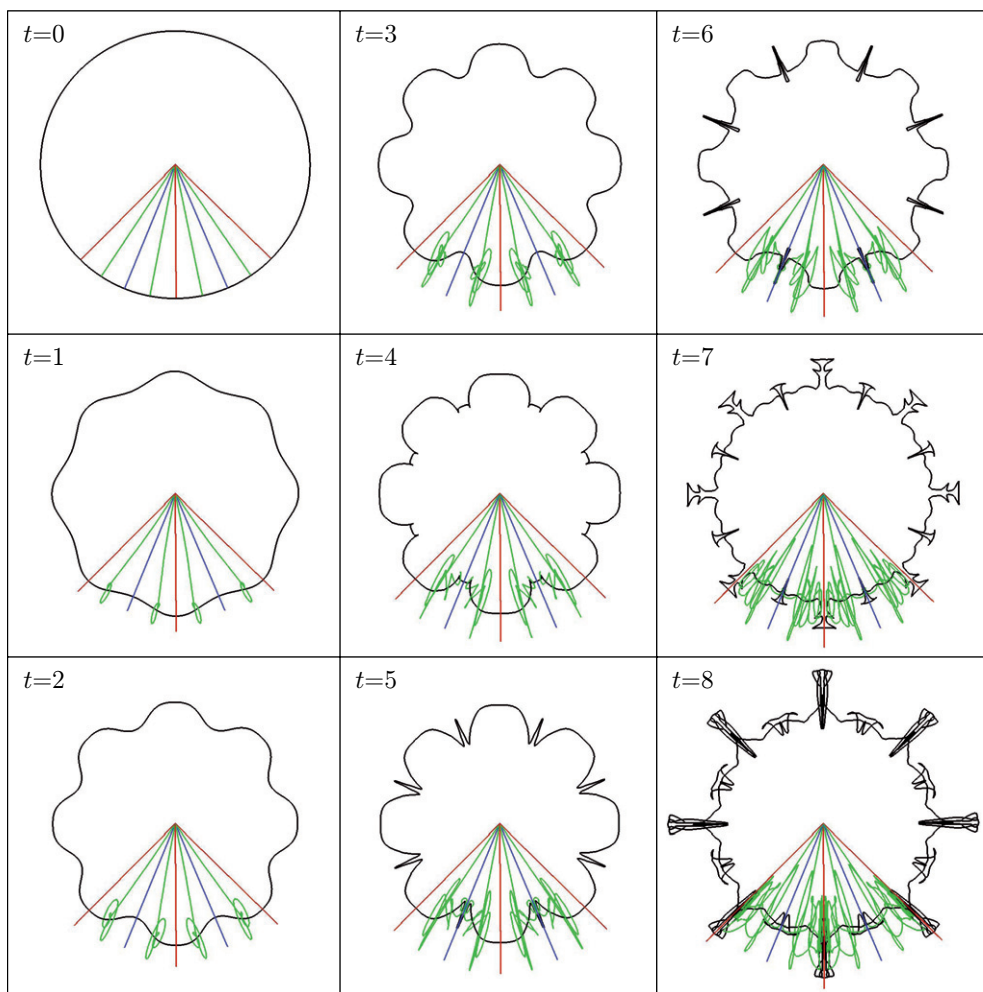
Figure 11. Core filament and rays, top view. The black line is the vortex filament at the edge of the sheet and the red, blue and green lines are material lines that were initially rays (radial line segments).

clarified by tracking material lines on the sheet surface. We observed two successive collapses of the vortex core, out of phase from each other by half an azimuthal wavelength and correlated with local axial flow converging to the collapse locations. At late times a sequence of ringlets is ejected radially from the core. Some features were found to resemble recent experimental findings on vortex rings, for example by Naitoh *et al* (2002) on axial flow in the core of the ring and by Dazin *et al* (2006a, 2006b) on dipole structures around the periphery of the ring.

There are several directions for future work. The proposed quadrature scheme amounts to a 2D trapezoid rule and it may be worthwhile to increase the order of accuracy by tracking more particles on each panel. The panel refinement scheme is effective in resolving the sheet's roll-up, stretching and folding, but it is not well suited for regions where the sheet is twisting. The twisting is an obstacle to further progress and may require a remeshing scheme. However instead of resetting the particles to lie on a regular mesh, it may be possible to retain the
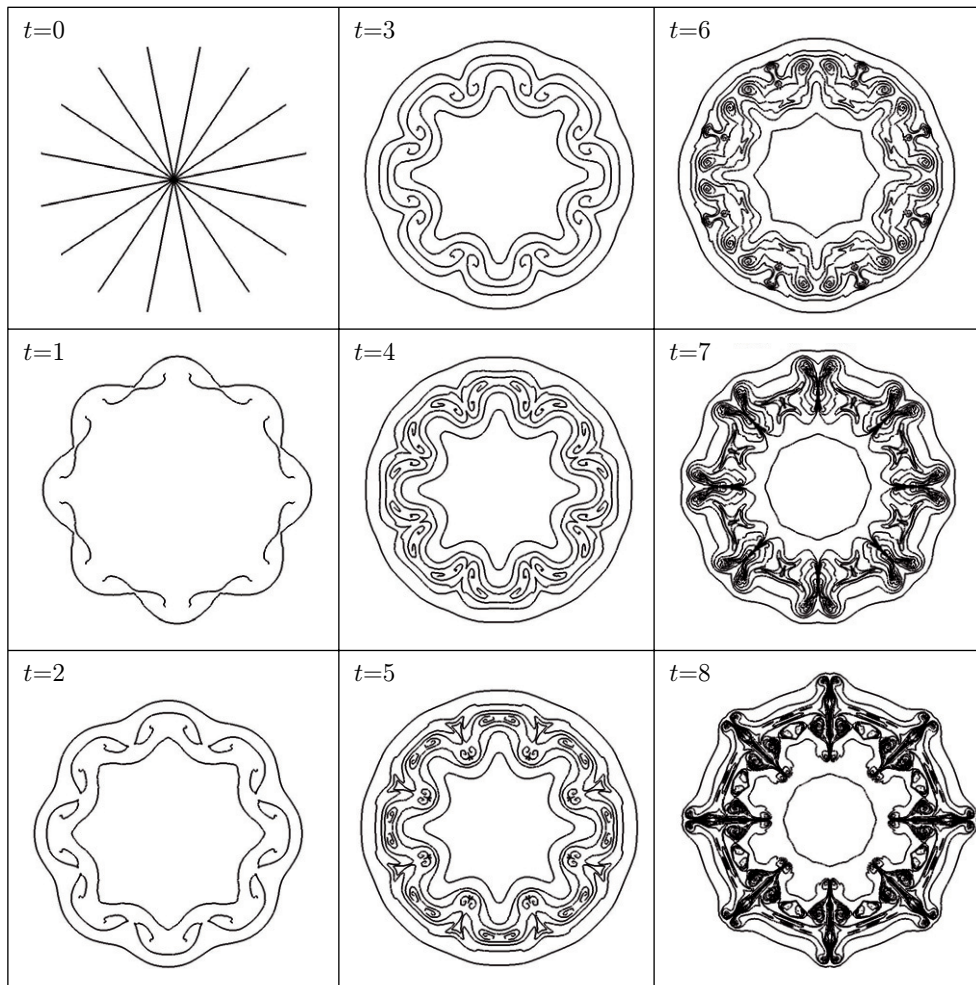
Figure 12. Horizontal slices through vortex core, top view.

particles and instead redefine the panels, although the details of such a scheme remain to be worked out.

Another goal is to simulate vortex ring formation from a wavy orifice (e.g. Naitoh *et al* 2002) or an inclined nozzle (e.g. Lim 1998, Webster and Longmire 1998), including the separation process. This would eliminate the need to impose an ad hoc initial perturbation in the simulation and might be done by coupling the present 3D vortex sheet method with an extension of the axisymmetric separation model of Nitsche and Krasny (1994). Their work was influenced by the experimental study of Didden (1979) on separation at the edge of a circular nozzle. The corresponding experiments for the case of a non-circular nozzle will be of great value in guiding future simulations of vortex rings.

Acknowledgments

References

Agishtein M E and Migdal A A 1989 Dynamics of vortex surfaces in three dimensions: theory and simulations *Physica* D **40** 91–118

Archer P J, Thomas T G and Coleman G N 2008 Direct numerical simulation of vortex ring evolution from the laminar to the early turbulent regime *J. Fluid Mech.* **598** 201–26

Ashurst W T and Meiburg E 1988 Three-dimensional shear layers via vortex dynamics *J. Fluid Mech.* **189** 87–116

Bergdorf M, Koumoutsakos P and Leonard A 2007 Direct numerical simulations of vortex rings at $Re_\Gamma = 7500$ *J. Fluid Mech.* **581** 495–505

Brady M, Leonard A and Pullin D I 1998 Regularized vortex sheet evolution in three dimensions *J. Comput. Phys.* **146** 520–45

Caflisch R E 1988 Mathematical analysis of vortex dynamics *Mathematical Aspects of Vortex Dynamics* ed R E Caflisch (Leesburg, VA: SIAM) pp 1–24

Chorin A J and Bernard P S 1973 Discretization of a vortex sheet with an example of roll-up *J. Comput. Phys.* **13** 423–9

Cocle R, Winckelmans G and Daeninck G 2008 Combining the vortex-in-cell and parallel fast multipole methods for efficient domain decomposition simulations *J. Comput. Phys.* **227** 9091–120

Cottet G-H and Koumoutsakos P D 2000 *Vortex Methods: Theory and Practice* (Cambridge: Cambridge University Press)

Dazin A, Dupont P and Stanislas M 2006a Experimental characterization of the instability of the vortex ring. Part I: Linear phase *Exp. Fluids* **40** 383–99

Dazin A, Dupont P and Stanislas M 2006b Experimental characterization of the instability of the vortex rings. Part II: Non-linear phase *Exp. Fluids* **41** 401–13

Didden N 1979 On the formation of vortex rings: rolling-up and production of circulation *Z. Angew. Math. Phys.* **30** 101–16

Feng H 2007 Vortex sheet simulations of 3D flows using an adaptive triangular panel/particle method *PhD Thesis* University of Michigan

Fukumoto Y and Hattori Y 2005 Curvature instability of a vortex ring *J. Fluid Mech.* **526** 77–115

Glezer A and Coles D 1990 An experimental study of a turbulent vortex ring *J. Fluid Mech.* **211** 243–83

Johnston H www.math.umass.edu/~johnston/newtreecode.html

Kaganovskiy L 2006 Hierarchical panel method for vortex sheet motion in three-dimensional flow *PhD Thesis* University of Michigan

Kaganovskiy L 2007 Adaptive panel representation for 3D vortex ring motion and instability *Math. Probl. Eng.* 68953 doi:10.1155/2007/68953

Kaneda Y 1990 A representation of the motion of a vortex sheet in a three-dimensional flow *Phys. Fluids* A **2** 458–61

Katz J and Plotkin A 2001 *Low-Speed Aerodynamics* (Cambridge: Cambridge University Press)

Knio O M and Ghoniem A F 1990 Numerical study of a three-dimensional vortex method *J. Comput. Phys.* **86** 75–106

Krasny R 1987 Computation of vortex sheet roll-up in the Trefftz plane *J. Fluid Mech.* **184** 123–55

Lim T T 1998 On the breakdown of vortex rings from inclined nozzles *Phys. Fluids* **10** 1666–71

Lim T T and Nickels T B 1995 Vortex rings *Fluid Vortices* ed S I Green (Dordrecht: Kluwer) pp 95–153

Lindsay K and Krasny R 2001 A particle method and adaptive treecode for vortex sheet motion in three-dimensional flow *J. Comput. Phys.* **172** 879–907

Maxworthy T 1977 Some experimental studies of vortex rings *J. Fluid Mech.* **81** 465–95

Moore D W 1972 Finite amplitude waves on aircraft trailing vortices *Aeronaut. Q.* **23** 307–314

Moore D W and Saffman P G 1975 The instability of a straight vortex filament in a strain field *Proc. R. Soc. Lond.* A **346** 413–25

Naitoh T, Fukuda N, Gotoh T, Yamada H and Nakajima K 2002 Experimental study of axial flow in a vortex ring *Phys. Fluids* **14** 143–9

Nitsche M and Krasny R 1994 A numerical study of vortex ring formation at the edge of a circular tube *J. Fluid Mech.* **216** 139–61

Pozrikidis C 2000 Theoretical and computational aspects of the self-induced motion of three-dimensional vortex sheets *J. Fluid Mech.* **425** 335–66

Rosenhead L 1930 The spread of vorticity in the wake behind a cylinder *Proc. R. Soc. Lond.* A **127** 590–612

Saffman P G 1978 The number of waves on unstable vortex rings *J. Fluid Mech.* **84** 625–39

Sakajo T 2001 Numerical computation of a three-dimensional vortex sheet in a swirl flow *Fluid Dyn. Res.* **28** 423–48

Shariff K and Leonard A 1992 Vortex rings *Annu. Rev. Fluid Mech.* **24** 235–79

Shariff K, Verzicco R and Orlandi P 1994 A numerical study of 3-dimensional vortex ring instabilities—viscous corrections and early nonlinear stage *J. Fluid Mech.* **279** 351–75

Stock M J 2006 A regularized inviscid vortex sheet method for three dimensional flows with density interfaces *PhD Thesis* University of Michigan

Stock M J, Dahm W J A and Tryggvason G 2008 Impact of a vortex ring on a density interface using a regularized inviscid vortex sheet method *J. Comput. Phys.* **227** 9021–43

Taylor G I 1953 Formation of a vortex ring by giving an impulse to a circular disc and then dissolving it away *J. Appl. Phys.* **24** 104–5

Webster D R and Longmire E K 1998 Vortex rings from cylinders with inclined exits *Phys. Fluids* **10** 400–16

Weigand A and Gharib M 1994 On the decay of a turbulent vortex ring *Phys. Fluids* **6** 3806–8

Widnall S E and Tsai C Y 1977 The instability of the thin vortex ring of constant vorticity *Phil. Trans. R. Soc.* A **287** 273–305